A Higher-Order Projection Method for the Simulation of Unsteady Turbulent Nonpremixed Combustion in an Industrial Burner *

Richard B. Pember, Ann S. Almgren, John B. Bell,
Phillip Colella, Louis Howell, and Mindy Lai
Lawrence Livermore National Laboratory

send all correspondence to:
Richard B. Pember
Lawrence Livermore National Laboratory
P.O. Box 808, L-316
Livermore, CA 94550 USA
Phone: (510)422-3721
e-mail: pember@llnl.gov
fax: (510)423-2993

Preference: Oral Presentation
Code Numbers: 8.1, 9.2, 3.7

1 Introduction

The modeling of transient effects in burners is becoming increasingly important. The problem of ensuring the safe performance of an industrial burner, for example, is much more difficult during the startup or shutdown phases of operation. The peak formation of pollutants is also much more dependent on transient behavior, in particular, on peak temperatures, than on average operating conditions.

In this paper we present a new methodology for the modeling of unsteady, nonpremixed, reacting flow in industrial burners. The algorithm uses a second-order projection method for unsteady, low-Mach number reacting flow [23] and accounts for species diffusion, convective and radiative heat transfer, viscous transport, turbulence, and chemical kinetics. The time step used by the method is restricted solely

*This work was performed under the auspices of the U.S. Department of Energy by the Lawrence Livermore National Laboratory under contract W-7405-Eng-48. Support under contract W-7405-Eng-48 was provided by the Applied Mathematical Sciences Program and the HPCC Grand Challenge Program of the Office of Scientific Computing at DOE. Dr. Colella is also partially supported by DARPA and the National Science Foundation under grant DMS-8919074; and by a National Science Foundation Presidential Young Investigator award under grant ACS-8958522; and by the Department of Energy High Performance Computing and Communications Program under grant DE-FGO3-92ER25140.

by an advective CFL condition. The methodology is applicable only in the low-Mach number regime ($M < .3$), typically met in industrial burners. The projection method for low-Mach number reacting flow is an extension of a higher-order projection method for incompressible flow [9, 5, 3, 4] to the low-Mach number equations of reacting flow[27]. Our method is based on an approximate projection formulation [2]. Radiative transport is modeled using the discrete ordinates method [8, 25].

The main goal of this work is to introduce and investigate the simulation of burners using a higher-order projection method for low-Mach number combustion. As such, the methodology is applied here only to axisymmetric flow in gas-fired burners for which the boundaries can be aligned with a rectangular grid. The perfect gas law is also assumed. In addition, we use a one-step reduced kinetics mechanism[22], a $k - \epsilon$ model for turbulent transport[20], and a simple turbulent combustion model[6, 26].

The higher-order projection method is a time-marching, predictor-corrector scheme. The predictor uses a sequential formulation, and, consequently, compatibility between the continuity equation and the equation of state cannot be guaranteed [33]. We introduce a technique to account for this based on similar approaches used in petroleum reservoir simulation [1, 35, 33].

There are a number of techniques for simulating reacting flow based on SIMPLE [30] and its extensions [16, 21]. Our method is qualitatively similar to SIMPLE in that SIMPLE also uses a sequential formulation with velocity-pressure corrections based on a projection methodology [9, 19]. A projection method for low-Mach number combustion is also presented in [14].

In §2 the low-Mach number model for combustion is reviewed. The governing equations, the numerical algorithm, and numerical results are presented in §3, §4, and §5, respectively.

2 Model for Low-Mach Number Combustion

The system of equations considered in this paper is based on a model for low-Mach number combustion[27], which we now briefly review. (See Table 1 for the nomenclature.)

For flow in a spatially open domain the underlying assumption in the low-Mach number model is that M is sufficiently small ($M < .3$) so that p can be written as the sum of a temporally and spatially constant part p_{amb} and a dynamic part π,

$$p(r, z, t) = p_{amb} + \pi(r, z, t), \tag{2.1}$$

where $\pi/p_{amb} = O\left(M^2\right)$. The momentum equation can then be written as

$$\rho\left(\frac{DU}{Dt} + G_{acc}(U)\right) = -\nabla\pi + \nabla \cdot \tau. \tag{2.2}$$

All thermodynamic quantities are considered to be independent of π. The perfect gas law for a multi-component gas in a flow satisfying the low-Mach number assumption

A	frequency in Arrhenius law
A'	turbulent combustion model constant
$C_\mu,\ C_1,\ C_2,\ \sigma_k,\ \sigma_\epsilon$	constants in $k-\epsilon$ model
$c_{p,l}(T)$	specific heat of species l at $p = p_{amb}$
$c_{p,mix}(T)$	specific heat of the gas mixture at $p = p_{amb}$
D_{in}	diameter of inlet
$D,\ D_t$	molecular, turbulent mass diffusion coefficients
E_a	activation energy in Arrhenius law
ϵ	turbulent kinetic energy dissipation rate
G	rate of production of turbulent kinetic energy
G_{acc}	vector of lower order acceleration terms
H_{fu}	net heat of reaction per unit mass of fuel
$h_l(T)$	specific enthalpy of species l at $p = p_{amb}$
in	subscript denoting an inlet value
k	turbulent kinetic energy
$k,\ k_t$	molecular, turbulent thermal conductivity
$k_\alpha,\ k_s$	absorption, scattering coefficients
l	subscript denoting species, fu (fuel), ox (oxidizer), $l = pr$ (product)
M	Mach number
m_l	mass fraction of species l
$\mu,\ \mu_t$	molecular, turbulent viscosity
μ_e	effective viscosity $= \mu + \mu_t$
mw_l	molecular weight of species l
p	pressure
π	dynamic pressure
p_{amb}	ambient pressure
q_{rad}	radiative heat flux
$\mathcal{R}$	universal gas constant
r	radial coordinate
R_{fu}	specific mass rate of fuel consumption
R_{ij}	Reynolds stress tensor
R_{mix}	gas constant of mixture
ρ	density
S	right hand side of the divergence constraint
σ	Stefan-Boltzmann constant
$\sigma_l,\ \sigma_t$	laminar, turbulent Prandtl numbers
st_l	mass of species l consumed in reaction per mass of fuel consumed
T	temperature
τ	stress tensor
τ_{lam}	laminar stress tensor
U	velocity $= (u, v, w)$; also (u, v) in some contexts
u, v, w	radial, axial, tangential components of velocity
w	subscript denoting a value at the wall
z	axial coordinate

Table 1: Nomenclature: Physical Model

is

$$\rho = \frac{p_{amb}}{R_{mix}T}, \tag{2.3}$$

where

$$R_{mix} = \mathcal{R}\sum_l \frac{m_l}{mw_l}.$$

Differentiating with respect to time,

$$\frac{D\rho}{Dt} = -\rho\left(\frac{1}{T}\frac{DT}{Dt} + \frac{1}{R_{mix}}\frac{DR_{mix}}{Dt}\right)$$

From continuity,

$$\frac{D\rho}{Dt} = -\rho\nabla\cdot U, \tag{2.4}$$

and the following constraint on the divergence of the velocity is obtained:

$$\nabla\cdot U = \frac{\rho}{p_{amb}}\left(\frac{DT}{Dt}R_{mix} + T\mathcal{R}\sum_l \frac{1}{mw_l}\frac{Dm_l}{Dt}\right) \equiv S. \tag{2.5}$$

A more general expression can be obtained if the perfect gas law is not satisfied.

The equations for low-Mach number combustion then consist of (2.5), (2.2), and the evolution equations for the other relevant quantities. To close the system of equations, the divergence constraint is used to derive an equation for π. We define $\frac{\partial U^*}{\partial t}$ by

$$\frac{\partial U^*}{\partial t} \equiv -(U\cdot\nabla)U - G_{acc}(U) + \frac{1}{\rho}\nabla\cdot\tau.$$

We can then uniquely define an operator $\boldsymbol{P}$ which decomposes $\frac{\partial U^*}{\partial t}$ into one part which satisfies the divergence constraint and a second which equals $(1/\rho)\nabla\pi$:

$$\frac{\partial U^*}{\partial t} = \boldsymbol{P}\left(\frac{\partial U^*}{\partial t}\right) + (\boldsymbol{I}-\boldsymbol{P})\frac{\partial U^*}{\partial t} \tag{2.6}$$

$$\frac{\partial U}{\partial t} = \boldsymbol{P}\left(\frac{\partial U^*}{\partial t}\right)$$

$$\frac{1}{\rho}\nabla\pi = (\boldsymbol{I}-\boldsymbol{P})\frac{\partial U^*}{\partial t}$$

$$\nabla\cdot\frac{\partial U}{\partial t} = \frac{\partial S}{\partial t} \tag{2.7}$$

where $\frac{\partial S}{\partial t}$ is defined from (2.5). Acoustic wave propagation has thus been effectively eliminated. Equivalently, let π_0 be a guess to the pressure field, and define

$$\delta = \pi - \pi_0. \tag{2.8}$$

π and $\frac{\partial U}{\partial t}$ then satisfy

$$\begin{aligned}
\delta &= \left(\nabla \cdot \frac{1}{\rho}\nabla\right)^{-1}\left(\nabla \cdot \left(\frac{\partial U^*}{\partial t} - \frac{1}{\rho}\nabla\pi_0\right) - \frac{\partial S}{\partial t}\right) \\
\pi &= \pi_0 + \delta \\
\frac{\partial U}{\partial t} &= \boldsymbol{P}\left(\frac{\partial U^*}{\partial t} - \frac{1}{\rho}\nabla\pi_0\right) \\
&= \left(\frac{\partial U^*}{\partial t} - \frac{1}{\rho}\nabla\pi_0\right) - \frac{1}{\rho}\nabla\delta. \qquad (2.9)
\end{aligned}$$

Equation (2.9) with the time derivatives for U, U^*, and S replaced by the quantities themselves provides a method for computing a velocity U field that satisfies the divergence constraint from an arbitrary velocity field U^*. π has no meaning, however, in this formulation.

3 Governing equations

3.1 Evolution equations

In addition to the applicability of the low-Mach number combustion model, several assumptions are made in formulating the system of equations considered here. The gas is assumed to satisfy the perfect gas law (2.3). Fuel oxidation is represented by a single-step irreversible reaction mechanism,

$$\text{fuel} + \text{oxidizer} \rightarrow \text{product}.$$

Turbulent transport is governed by a form of the $k - \epsilon$ equations for compressible flow[20].

The system of governing differential equations thus consists of the divergence constraint (2.5) plus the following evolution equations for density, velocity, temperature, species concentrations, and turbulent kinetic energy and dissipation rate:

Continuity:

$$\frac{\partial \rho}{\partial t} + \nabla \cdot (\rho U) = 0. \qquad (3.1)$$

Velocity:

$$\rho\frac{DU}{Dt} + \rho G_{acc}(U) = \rho \begin{pmatrix} \frac{Du}{Dt} - \frac{w^2}{r} \\ \frac{Dv}{Dt} \\ \frac{Dw}{Dt} + \frac{uw}{r} \end{pmatrix} = -\nabla\pi + \nabla \cdot \tau \qquad (3.2)$$

where

$$\begin{aligned} \tau &= \tau_{lam} - R_{ij}, \\ \tau_{lam} &= \mu\left(\frac{\partial U_i}{\partial x_j} + \frac{\partial U_j}{\partial x_i} - \tfrac{2}{3}\delta_{ij}\nabla\cdot U\right), \text{ and} \\ -R_{ij} &= \mu_t\left(\frac{\partial U_i}{\partial x_j} + \frac{\partial U_j}{\partial x_i} - \tfrac{2}{3}\delta_{ij}\nabla\cdot U\right) - \tfrac{2}{3}\delta_{ij}\rho k. \end{aligned} \tag{3.3}$$

Temperature:

$$\begin{aligned} \rho c_{p,mix}\frac{DT}{Dt} &= \nabla\cdot\left(\left(k+k_t\right)\nabla T\right) - \nabla\cdot q_{rad} + H_{fu}R_{fu} \\ &\quad +\nabla\cdot\textstyle\sum_l \rho h_l(T)\left(D+D_t\right)\nabla m_l - \rho\sum_l \frac{Dm_l}{Dt}h_l(T), \end{aligned} \tag{3.4}$$

where $c_{p,mix} = \sum_l m_l c_{p,l}(T)$.

Species mass fractions:

$$\frac{\partial\left(\rho m_l\right)}{\partial t} + \nabla\cdot\left(\rho U m_l\right) = \nabla\cdot\left(\left(D+D_t\right)\rho\nabla m_l\right) - st_l R_{fu}. \tag{3.5}$$

Turbulent kinetic energy and dissipation:

$$\begin{aligned} \rho\frac{Dk}{Dt} &= \nabla\cdot\left(\left(\frac{\mu_t}{\sigma_k}+\mu\right)\nabla k\right) + \\ &\quad G - \frac{\mu_t}{\rho^2}\left(\nabla\rho\cdot\nabla p\right) - \rho\epsilon \end{aligned} \tag{3.6}$$

$$\begin{aligned} \rho\frac{D\epsilon}{Dt} &= \nabla\cdot\left(\left(\frac{\mu_t}{\sigma_\epsilon}+\mu\right)\nabla\epsilon\right) + \\ &\quad C_1\frac{\epsilon}{k}\left(G - \frac{\mu_t}{\rho^2}\left(\nabla\rho\cdot\nabla p\right)\right) - C_2\rho\frac{\epsilon^2}{k} \end{aligned} \tag{3.7}$$

where

$$G = -R_{ij}\frac{\partial U_i}{\partial x_j}. \tag{3.8}$$

The turbulent viscosity, thermal conductivity, and mass diffusivity are defined by

$$\mu_t = C_\mu\rho\frac{k^2}{\epsilon}, \qquad k_t = \frac{c_{p,mix}\mu_t}{\sigma_t}, \qquad D_t = \frac{\mu_t}{\rho\sigma_t}$$

while the standard values of the turbulence model constants [20] are used:

$$C_\mu = .09,\ C_1 = 1.44,\ C_2 = 1.92,\ \sigma_k = 1.0,\ \sigma_\epsilon = 1.3,\ \sigma_t = .7.$$

Note that a Lewis number of 1.0 is assumed so that σ_t also represents the turbulent Schmidt number.

The combustion model is based on the model in [22]. The value of R_{fu} is the smaller of two rates, given by an Arrhenius rate equation and an eddy-dissipation model [6, 26], respectively:

$$R_{fu} = \min\left(\rho^2 m_{fu} m_{ox} A\,\exp\left(-E_a/\mathcal{R}T\right), R_{fu,turb}\right) \tag{3.9}$$

where

$$R_{fu,turb} = \frac{\epsilon}{k} \min \left(A' \rho m_{fu}, A' \rho m_{ox} / st_{ox} \right). \tag{3.10}$$

Values of A' from 2 to 32 have been reported [6]. $A' = 4.0$ is recommended in [26].

The divergence of the radiative heat flux q_{rad} is found using a discrete ordinates model. The discrete ordinates model [8, 25] defines $\nabla \cdot q_{rad}$ by

$$\nabla \cdot q_{rad} = 4 k_a \sigma T^4 - k_a \sum_{p,q} w_{p,q} I_{p,q}, \tag{3.11}$$

where the subscript p identifies a level of ordinate directions with a particular value of ξ, and q indexes the separate ordinates sharing that level. $I_{p,q}$ satisfies

$$\frac{\mu_{p,q}}{r} \frac{\partial (r I_{p,q})}{\partial r} + \xi_p \frac{\partial I_{p,q}}{\partial z} - \frac{1}{r} \frac{\partial (\eta I)}{\partial \omega} + (k_a + k_s) I_{p,q} = k_a \frac{\sigma T^4}{\pi} + \frac{k_s}{4\pi} \sum_{p',q'} w_{p',q'} I_{p',q'} \tag{3.12}$$

where $\sum_{p,q} w_{p,q} = 4\pi$ and μ, ξ, and η denote direction cosines.

3.2 Boundary conditions

The inlet profiles of velocity, temperature, and species have prescribed values. In the examples presented later, we use the inlet values for the turbulent kinetic energy and dissipation rate recommended in [18] and [22], respectively:

$$k_{in} = .005 v_{in}^2, \ \epsilon_{in} = c_\mu k_{in}^{3/2} / (.03 D_{in}). \tag{3.13}$$

At the outflow boundary, the gradients of velocity, temperature, species concentrations, and turbulent quantities are set to zero.

At solid walls, the velocity and the gradients of ρ, m_l and k are set to zero. The temperature is a prescribed value. Near the wall, however, the treatments of the dissipation rate, the components of τ acting in directions tangential to the wall, and the conductive heat flux $(k + k_t)\nabla T$ must be modified, given that the boundary layer is not resolved [24, 21, 31]. These modifications are often referred to as "using the law-of-the-wall". Computationally, these are applied only in the cells bordering the wall. ϵ is defined by

$$\epsilon = c_\mu^{3/4} k^{3/2} / \kappa y \tag{3.14}$$

where y is the distance to the wall [32]. A non-dimensionalized distance from the wall, y^+ is computed by

$$y^+ = y \rho c_\mu^{1/4} k^{1/2} / \mu.$$

If y^+ is less than a cutoff value (typically, 11.225 [10]), the laminar part of the shear stress and the heat flux, i.e., τ_{lam} and $k \nabla T$, alone are used. Otherwise, at the wall the components of τ acting in the tangential direction are given by

$$\tau_w = \pm \frac{u \kappa c_\mu^{1/4} k^{1/2} \rho}{\ln (E y^+)} \tag{3.15}$$

i, j	cell indices in $r-$, $z-$ directions
Δr	cell width in r-direction
Δz	cell width in z-direction
Δt	time step used to advance solution from t^n to t^{n+1}
r_i	r-coordinate of center of cell ij
$r_{i+1/2}$	r-coordinate of upper r-edge of cell ij
$\tilde{S}$	right hand side of the numerical divergence constraint
t^n	time at the end of the n-th time step
$t^{n+1/2}$	$t^n + \Delta t/2$
$(\cdot)_{ij}^n$	value at center of cell ij at time t^n
$u_{ij}^{n+1,*}, v_{ij}^{n+1,*}$	axial and radial components of velocity before enforcement of divergence constraint
$(\cdot)_{ij}^{n+1,p}$	predicted value at center of cell ij at time t^n
$(\cdot)_{ij}^{n+1/2}$	value at center of cell ij at time $t^n + \Delta t/2$
$(\cdot)_{i+1/2,j}^{n+1/2}$	value at upper r-edge of cell ij at time $t^n + \Delta t/2$
$(\cdot)_{i,j+1/2}^{n+1/2}$	value at upper z-edge of cell ij at time $t^n + \Delta t/2$
$(\cdot)_{i+1/2,j+1/2}^{n+1/2}$	value at upper corner of cell ij at time $t^n + \Delta t/2$
$(\cdot)_{ij}^{n+1}$	value at center of cell ij at time $t^n + \Delta t$

Table 2: Nomenclature: Numerical Algorithm

and the conductive heat flux is

$$q_w = \frac{c_{p,mix}\rho c_\mu^{1/4} k^{1/2}}{\frac{\sigma_t}{\kappa}\ln(Ey^+) + \sigma_t \frac{\pi/4}{\sin \pi/4}\left(\frac{A}{\kappa}\right)^{1/2}\left(\frac{\sigma_t}{\sigma_l} - 1\right)\left(\frac{\sigma_t}{\sigma_l}\right)^{1/4}}(T - T_w), \tag{3.16}$$

where u and T are the tangential component of velocity and temperature at distance y from the wall. A "+" or "−" sign is used in (3.15) at points "below" or "above" the wall, respectively. E, κ, and van Driest's constant A depend on the wall roughness. We use the values recommended in [21], 8.8, .42, and 26, respectively, and also assume $\sigma_t = \sigma_l$. The terms in (3.8) corresponding to τ_w must be replaced by τ_w^2/μ_e as appropriate.

The boundary conditions used in computing $\nabla \cdot q_{rad}$ are model-dependent. For the discrete ordinates model, we use the recommendations in [25].

4 Numerical algorithm

In this section we present a methodology for obtaining time-dependent solutions to the equations in §3.1. We assume a uniform grid of rectangular cells with widths Δr and Δz indexed by i and j. (See Table 2 for the nomenclature.) All flow quantities in the solution lie on whole time steps (t^n) and are cell-centered with the exception of pressures which lie on cell corners on lagged half-time steps ($t^{n-1/2}$).

The overall strategy of the algorithm in advancing the solution from time t^n to $t^n + \Delta t = t^{n+1}$ is that of a predictor-corrector scheme. In the predictor step,

values of k, ϵ, w, T, and m_l are computed at time t^{n+1}. In addition, values of u and v are predicted at t^{n+1}. The values of u and v do not necessarily satisfy the divergence constraint (2.5). In the corrector step, equation (2.9) is solved to impose this constraint and to update the value of π to $t^n + \Delta t/2$.

The predictor step of the algorithm is itself a multi-step algorithm. A predictor-corrector formulation is used within the predictor step so that second-order accuracy can be obtained. The predictor consists of the following steps:

(1) Compute Δt:

$$\Delta t = \sigma \min_{ij} \left(\frac{\Delta r}{u_{ij}^n}, \frac{\Delta z}{v_{ij}^n} \right) \tag{4.1}$$

where the CFL number σ satisfies $\sigma < 1$.

(2) Compute values of $u_{i+1/2,j}^{n+1/2}, v_{i+1/2,j}^{n+1/2}$ and $u_{i,j+1/2}^{n+1/2}, v_{i,j+1/2}^{n+1/2}$, at all $r-$ and $z-$ cell edges, respectively, using the higher-order Godunov scheme.

(3) Project edge velocities found in (2) so that they satisfy the divergence constraint.

(4) Compute values of $\varphi_{i+1/2,j}^{n+1/2}$ and $\varphi_{i,j+1/2}^{n+1/2}$ for $\varphi = w, \rho, \rho m_l, T, k$, and ϵ using the higher-order Godunov scheme.

(5) Form discrete approximations of convective terms, i.e.,

$$\begin{aligned} &(\nabla \cdot (\rho U \varphi))_{ij}^{n+1/2}, \text{ for } \varphi = 1, m_l, \text{ and} \\ &(U \cdot \nabla \varphi)_{ij}^{n+1/2} \text{ for } \varphi = u, v, w, T, k, \text{ and } \epsilon. \end{aligned}$$

(6) Compute $\rho_{ij}^{n+1} = \rho_{ij}^n + \Delta t \, (\nabla \cdot \rho U)_{ij}^{n+1/2}$.

(7) Predict values of flow quantities at t^{n+1}, $\varphi_{ij}^{n+1,p}$ for $\varphi = k, \epsilon, m_l, T, u, v, w$, using Crank-Nicholson differencing [13, 29] of the diffusive terms and, for m_l, the reactive terms as well.

(8) Compute $(\nabla \cdot q_{rad})_{ij}^{n+1}$ using $T_{ij}^{n+1,p}$.

(9) Compute values of flow quantities, φ_{ij}^{n+1} for $\varphi = k, \epsilon, m_l, T, w$, $u_{ij}^{n+1,*}$, and $v_{ij}^{n+1,*}$, at t^{n+1} using Crank-Nicholson differencing.

In steps (7) and (9) the equations for each of the flow quantities $k, \epsilon, m_i, T, u, v$, and w are solved sequentially in the order listed and the difference equations are formulated so that only linear systems of equations result from the Crank-Nicholson differencing. These linear systems and those arising in the projection steps are solved using the Gauss-Seidel scheme [13, 29] with multigrid acceleration[7].

In the remainder of this section we provide the details of the algorithm summarized above. Except as noted, standard discretizations of derivatives are used, and half-time and edge values are found by averaging.

4.1 Numerical Divergence Constraint and Temperature Equation

The continuity equation (3.1) and the equation of state (2.3) are redundant equations for the density ρ. Although the evolution equations with (3.1) replaced by (2.3)

analytically conserve mass [27], numerical conservation of mass cannot be guaranteed due to the sequential approach used in the predictor step [33]. We therefore use (3.1) instead of (2.3).

Using (3.1), however, makes it necessary to add an extra term to the discrete form of the divergence constraint (2.5) which accounts for the discrepancy between the values of ρ found by continuity and by the equation of state. The discrete divergence constraint is given by

$$\begin{aligned}(\nabla \cdot U)_{ij} &= \left(\frac{\rho}{\tilde{p}_{ij}}\left(\left(\frac{DT}{Dt}\right)R_{mix} + T\mathcal{R}\sum_l \frac{1}{mw_l}\left(\frac{Dm_l}{Dt}\right)\right)\right)_{ij} + \\ & \qquad f\left(\tilde{p}_{ij} - p_{amb}\right)\frac{c_{p,mix,ij} - R_{mix,ij}}{\Delta t c_{p,mix,ij}\tilde{p}_{ij}} \equiv \tilde{S}_{ij},\end{aligned} \tag{4.2}$$

where $f = .5$ and $\tilde{p}_{ij} = R_{mix,ij}\rho_{ij}T_{ij}$.

The discrete form of the equation for T requires modification so that it is consistent with (4.2):

$$\begin{aligned}\left(\rho c_{p,mix}\frac{DT}{Dt}\right)_{ij} &= \left(\nabla\cdot\left(\left(k + k_t\right)\nabla T\right) - \nabla\cdot q_{rad} + H_{fu}R_{fu}\right. \\ & \quad \left. + \nabla\cdot\sum_l \rho h_l(T)\left(D + D_t\right)\nabla m_l - \rho\sum_l \frac{Dm_l}{Dt}h_l(T)\right)_{ij} - \\ & \quad f\frac{\tilde{p}_{ij} - p_{amb}}{\Delta t}.\end{aligned} \tag{4.3}$$

The term $(\tilde{p}_{ij} - p_{amb})/\Delta t$ acts to drive the solution back to the constraint $\tilde{p}_{ij} = p_{amb}$. Similar treatments have been used in numerical petroleum reservoir simulation [1, 35, 33].

4.2 Predictor

4.2.1 Computation of Edge Velocities at $t^{n+1/2}$

The computation of $(u,v)^{n+1/2}_{i+1/2,j} \equiv U^{n+1/2}_{i+1/2,j}$ and $(u,v)^{n+1/2}_{i,j+1/2} \equiv U^{n+1/2}_{i,j+1/2}$ is a variant [4, 3] of the higher-order upwind method in [12]. The method consists of two general steps:

(1) The calculation of time-centered left and right edge states, $U^{n+1/2}_{i+1/2,j,L}$ and $U^{n+1/2}_{i+1/2,j,R}$, at all r-cell faces and bottom and top edge states, $U^{n+1/2}_{i,j+1/2,B}$ and $U^{n+1/2}_{i,j+1/2,T}$, at all z-cell faces.

(2) The calculation of time-centered edge states $U^{n+1/2}_{i+1/2,j}$ at all r-cell faces and $U^{n+1/2}_{i,j+1/2}$ at all z-cell faces by an upwinding procedure.

In step (1) cell edge values at $t^{n+1/2}$ are computed using Taylor's theorem and the differential equation (3.2). For edge $(i+1/2, j)$ this yields

$$\begin{aligned}U^{n+1/2,L}_{i+1/2,j} &= U^n_{ij} + \left(\frac{\Delta x}{2} - \frac{u_{ij}\Delta t}{2}\right)U^n_{x,ij} - \frac{\Delta t}{2}\left(\widehat{vU_y}\right)_{ij} \\ & \quad + \frac{1}{\rho^n_{ij}}\frac{\Delta t}{2}\left(-G_{acc}(U^n_{ij}) - (\nabla\pi)^{n-1/2}_{ij} + (\nabla\cdot\tau)^n_{ij}\right)\end{aligned} \tag{4.4}$$

and

$$\begin{aligned} U^{n+1/2,R}_{i+1/2,j} &= U^n_{i+1,j} - \left(\frac{\Delta x}{2} + \frac{u_{i+1,j}\Delta t}{2}\right) U^n_{x,i+1,j} - \frac{\Delta t}{2}\left(\widehat{vU_y}\right)_{i+1,j} \\ &\quad + \frac{1}{\rho^n_{i+1,j}}\frac{\Delta t}{2}\left(-G_{acc}(U^n_{i+1,j}) - (\nabla\pi)^{n-1/2}_{i+1,j} + (\nabla\cdot\tau)^n_{i+1,j}\right). \end{aligned} \tag{4.5}$$

Similar expressions are used to predict values at the other cell edges. First-order derivatives normal to the edge (in this case U_x) are evaluated using monotonicity-limited fourth-order slope approximations [11].

The transverse derivative terms ($\widehat{vU_y}$ in this case) are evaluated as in [3]. Specifically, we define

$$\begin{aligned} \widehat{U}^B_{i,j+1/2} &= U^n_{ij} + \left(\frac{\Delta y}{2} - \frac{v_{ij}\Delta t}{2}\right) U^n_{y,ij}, \\ \widehat{U}^T_{i,j+1/2} &= U^n_{i,j+1} - \left(\frac{\Delta y}{2} + \frac{v_{i,j+1}\Delta t}{2}\right) U^n_{y,i,j+1}, \end{aligned} \tag{4.6}$$

where U_y are limited slopes in the y direction, with similar expressions for the lower edge of i,j. We then define the normal advective velocity on the edge:

$$\widehat{v}^{adv}_{i,j+1/2} = \begin{cases} \widehat{v}^B_{i,j+1/2} & \text{if } \widehat{v}^B_{i,j+1/2} > 0, \quad \widehat{v}^B_{i,j+1/2} + \widehat{v}^T_{i,j+1/2} > 0 \\ 0 & \text{if } \widehat{v}^B_{i,j+1/2} \le 0, \widehat{v}^T_{i,j+1/2} \ge 0 \text{ or } \widehat{v}^B_{i,j+1/2} + \widehat{v}^T_{i,j+1/2} = 0 \\ \widehat{v}^T_{i,j+1/2} & \text{if } \widehat{v}^T_{i,j+1/2} < 0, \quad \widehat{v}^B_{i,j+1/2} + \widehat{v}^T_{i,j+1/2} < 0 \end{cases}$$

We next find $\widehat{U}^{i,j+1/2}$ by an upwind procedure:

$$\widehat{U}_{i,j+1/2} = \begin{cases} \widehat{U}^B_{i,j+1/2} & \text{if } \widehat{v}^{adv}_{i,j+1/2} > 0 \\ 1/2(\widehat{U}^B_{i,j+1/2} + \widehat{U}^T_{i,j+1/2}) & \text{if } \widehat{v}^{adv}_{i,j+1/2} = 0 \\ \widehat{U}^T_{i,j+1/2} & \text{if } \widehat{v}^{adv}_{i,j+1/2} < 0. \end{cases} \tag{4.7}$$

$\widehat{U}_{i,j-1/2}$ is found in a similar manner. These values are then used to form the transverse derivative in (4.4):

$$(\widehat{vU_y})_{ij} = 1/2(\widehat{v}^{adv}_{i,j+1/2} + \widehat{v}^{adv}_{i,j-1/2})(\widehat{U}_{i,j+1/2} - \widehat{U}_{i,j-1/2}).$$

In step (2) a procedure similar to (4.7) is used to compute $U^{n+1/2}_{i+1/2,j}$. $U^{n+1/2}_{i,j+1/2}$ is constructed in a similar fashion.

4.2.2 Projection of Normal Edge Velocities.

In this step we use a MAC projection [19, 3] to enforce the divergence constraint (4.2). The equation

$$\left(D^{MAC}\frac{1}{\rho^n}G^{MAC}\phi\right)_{ij} = \left(D^{MAC}U^{n+1/2}\right)_{ij} - \tilde{S}^n_{ij}$$

is solved for ϕ, where $\tilde{S}^n$ is given by (4.2), and D^{MAC} and G^{MAC} are standard discretizations of the divergence and gradient operators on a staggered grid.

The edge velocities are then corrected by

$$\begin{aligned} u^{n+1/2}_{i+1/2,j} &:= u^{n+1/2}_{i+1/2,j} - \frac{1}{\rho^n_{i+1/2,j}}(G^{MAC}\phi)^r_{i+1/2,j} \\ v^{n+1/2}_{i,j+1/2} &:= v^{n+1/2}_{i,j+1/2} - \frac{1}{\rho^n_{i,j+1/2}}(G^{MAC}\phi)^z_{i,j+1/2}. \end{aligned} \tag{4.8}$$

4.2.3 Formation of convective derivatives.

The values of $\varphi^{n+1/2}_{i+1/2,j}$, $\varphi^{n+1/2}_{i,j+1/2}$ for $\varphi = w,\ \rho,\ \rho m_l$ $(l = fu,\ ox)$, T, k, and ϵ are computed using a procedure similar to that in §4.2.1 except that the upwind states are computed using the edge velocities from (4.8). The discrete approximations to the convective derivatives are then formed using central differences of $\varphi^{n+1/2}_{i+1/2,j}$ and $\varphi^{n+1/2}_{i,j+1/2}$.

4.2.4 Crank-Nicholson Differencing

In steps (7) and (9) of the predictor we solve difference equations obtained by applying the Crank-Nicholson method to the governing equations. In writing the difference equations below, we use ψ to represent all other flow quantities. ψ also includes $\nabla \cdot U$, which is evaluated using (2.5).

The difference equation for (u, v) is

$$\begin{aligned} \rho^{n+1/2}_{ij} \begin{pmatrix} \dfrac{u^{n+1,*}_{ij} - u^n_{ij}}{\Delta t} + ((u,v)\cdot\nabla u)^{n+1/2}_{ij} - \tfrac{1}{2}\dfrac{\left(w^{n+1,p}_{ij}\right)^2 + \left(w^n_{ij}\right)^2}{r_i} \\ \dfrac{v^{n+1,*}_{ij} - v^n_{ij}}{\Delta t} + ((u,v)\cdot\nabla v)^{n+1/2}_{ij} \end{pmatrix} = \\ -(\nabla\pi)^{n-1/2}_{ij} + \frac{L_h\left(u^{n+1,*}, v^{n+1,*}, \psi^{n+1,p}\right) + L_h\left(u^n, v^n, \psi^n\right)}{2}. \end{aligned} \tag{4.9}$$

where L_h is the discretization of the first two rows of $\nabla \cdot \tau$ in (3.2).

The difference equations for k, ϵ, T, m_l, and w are similar. The equations for m_l also account for potential stiffness in the R_{fu} term.

In step (7) of the predictor, step n values are used for the predicted values and half-time values. In step (9), step $n+1$ values of $\varphi = k, \epsilon$, and m_l are used for the predicted values in computing subsequent quantities (e.g., k^{n+1} in computing $\epsilon^{n+1}, u^{n+1,*}$, and $v^{n+1,*}$) in order that proper coupling is obtained. However, consistent values of m_l are used in all approximations of R_{fu}.

4.2.5 Computation of $\nabla \cdot q_{rad}$.

We discretize (3.12) as a conservation relation for each cell[8, 25] and use diamond-difference formulae with flux-limiting. The temperature field $T^{n+1,p}_{ij}$ is used. The

system is solved by successive sweeps through the mesh for each ordinate direction. In the computations for this paper we set both reflection and scattering to zero. The ordinate values are taken from the S_6 set listed in [15].

4.3 Corrector

In this step, we perform an approximate projection [2] in order to enforce the divergence constraint (4.2) and find $\pi^{n+1/2}$. In the following, D_a and G_a are standard discretizations of the divergence and the gradient operators. We solve the difference equations

$$(L\delta)_{i+1/2,j+1/2} = \left(D_a \left(\frac{U^{n+1,*} - U^n}{\Delta t} \right) \right)_{i+1/2,j+1/2} - \frac{\tilde{S}^{n+1,p}_{i+1/2,j+1/2} - \tilde{S}^n_{i+1/2,j+1/2}}{\Delta t}. \tag{4.10}$$

For $\Delta r = \Delta z$,
$(L\delta)_{i+1/2,j+1/2} = \frac{1}{6 r_{i+1/2} \Delta r^2}$

$$\begin{aligned}
&\Big(\sigma_{ij}(2\delta_{i-1/2,j-1/2} + \delta_{i+1/2,j-1/2} + \delta_{i-1/2,j+1/2} - 4\delta_{i+1/2,j+1/2}) + \\
&\sigma_{i,j+1}(2\delta_{i-1/2,j+3/2} + \delta_{i+1/2,j+3/2} + \delta_{i-1/2,j+1/2} - 4\delta_{i+1/2,j+1/2}) + \\
&\sigma_{i+1,j}(2\delta_{i+3/2,j-1/2} + \delta_{i+1/2,j-1/2} + \delta_{i+3/2,j+1/2} - 4\delta_{i+1/2,j+1/2}) + \\
&\sigma_{i+1,j+1}(2\delta_{i+3/2,j+3/2} + \delta_{i+1/2,j+3/2} + \delta_{i+3/2,j+1/2} - 4\delta_{i+1/2,j+1/2}) \Big)
\end{aligned} \tag{4.11}$$

where $\sigma_{ij} = r_i / \rho^{n+1/2}_{ij}$. U^{n+1}_{ij} is then computed by

$$U^{n+1}_{ij} = U^{n+1,*} - \frac{1}{\rho^{n+1/2}_{ij}} (G_a \delta)_{ij}$$

and $\pi^{n+1/2}_{i+1/2,j+1/2} = \pi^{n-1/2}_{i+1/2,j+1/2} + \delta$.

5 Numerical Results

We now discuss results from a simulation of a natural gas-air burner using the above methodology.

The physical properties used are the following. Polynomial curve fits are used for $c_{p,ox}$, $c_{p,pr}$ [34] and $c_{p,fu}$ [17]. Other properties are $A = 10^{10}\text{m}^3/(\text{kg-sec})$ and $E_a/\mathcal{R} = 1.84 \times 10^4$ °K [22], $H_{fu} = 4.855 \times 10^7 \text{J/kg}$ [34], and $k_a = .2\text{m}^{-1}$ [28]. Nominal, constant values of the laminar diffusion coefficients D, k and μ are used.

The geometry of the sample burner is shown in Figure 1. The initial conditions are quiescent and ambient except for a hot spot near the inlet. The inlet conditions are $T_{in} = 300°\text{K}$, $v_{in} = 12.2\text{m/sec}$, no radial velocity, and a tangential velocity profile for the air given by a swirl number of .5 and solid body rotation. The adiabatic flame temperature for our values of T_{in}, c_p and H_{fu} is 2268 °K.

The first two sets of results are for Arrhenius kinetics alone, i.e., A'" = "∞. Figure 2 shows results computed on a 32×128 grid at $t = 1.53$ sec. Temperature, velocity, and air mass fraction are displayed. Figure 3 shows the temperature computed on a 16×64 grid at $t = .075$, .152, .763, and 1.53 sec. The results at $t = 1.53$ sec for the two resolutions compare favorably, with the coarser grid showing a slightly higher maximum temperature.

Figure 4 shows the effect of the eddy-dissipation model on the temperature field at late time. The results using Arrhenius kinetics are included for comparison. The maximum temperatures displayed are 2191°K ($A' = \infty$), 2132°K ($A' = 32.0$), and 1780°K ($A' = 4.0$). A similar decrease in the maximum temperature when using the eddy-dissipation model was observed in [26].

6 Discussion

We have introduced a new methodology for computing time-dependent nonpremixed combustion in burners. The computational results appear reasonable and are consistent under grid refinement. Additional validation is in progress. The turbulent combustion model also warrants further investigation.

We are uncertain as to why the computations discussed in the previous section effectively reached steady state after the unreasonably short simulated time of 1.53 sec. One possible explanation is that buoyancy effects are neglected. A second is that rapid attainment of steady state conditions may be an artifact of the $k - \epsilon$ model.

Acknowledgements. We would like to thank Steve Londerville and Scott Drenan of Coen Company, Inc., for a number of helpful discussions during the course of this research.

References

[1] G. Acs, S. Doleschall, and E. Farkas. General purpose compositional model (SPE 10515). In *6th SPE Symposium on Reservoir Simulation.* New Orleans, LA, February, 1982, p.385-404.

[2] A.S. Almgren, J.B. Bell, and W.G. Szymczak. A numerical method for the incompressible Navier-Stokes equations based on an approximate projection. *SIAM J. Sci. Comput.*, accepted for publication. UCRL-JC-112842, Lawrence Livermore National Laboratory, January, 1993.

[3] J. B. Bell, P. Colella, and L. H. Howell. An efficient second-order projection method for viscous incompressible flow. In *10th AIAA Computational Fluid Dynamics Conference*, Honolulu, June 24–27, 1991.

[4] J. B. Bell and D. L. Marcus. A second-order projection method for variable-density flows. *J. Comput. Phys.*, 101:334–348, 1992.

[5] J.B. Bell, P. Colella, and H.M. Glaz. A second-order projection method for the incompressible Navier-Stokes equations. *J. Comput. Phys.*, 85:257–283, 1989.

[6] R.W. Bilger. Turbulent diffusion flames. *Ann. Rev. Fluid Mech.*, 21:101–135, 1989.

[7] W.L. Briggs. *A Multigrid Tutorial.* SIAM, Philadelphia, PA, 1987.

[8] B. G. Carlson and K. D. Lathrop. Transport theory—the method of discrete ordinates. In H. Greenspan, C. N. Kelber, and D. Okrent, editors, *Computing Methods in Reactor Physics*, pages 171–266. Gordon and Breach, New York, 1968.

[9] A. Chorin. Numerical solution of the Navier-Stokes equations. *Math. Comp.*, 22:745–762, 1969.

[10] M. Ciofalo and M.W. Collins. $k - \epsilon$ predictions of heat transfer in turbulent recirculating flows using an improved wall treatment. *Numer. Heat. Transfer, Part B*, 15:21–47, 1989.

[11] P. Colella. A direct Eulerian MUSCL scheme for gas dynamics. *SIAM J. Sci. Stat. Comput.*, 6:104–117, 1985.

[12] P. Colella. Multidimensional upwind methods for hyperbolic conservation laws. *J. Comput. Phys.*, 87:171–200, 1990.

[13] G. Dahlquist and A. Bjorck. *Numerical Methods.* Prentice-Hall, 1974.

[14] H. Dwyer. Calculation of low Mach number reacting flows. *AIAA Journal*, 28(1):98–105, 1990.

[15] W. A. Fiveland. Discrete-ordinates solutions of the radiative transport equation for rectangular enclosures. *J. Heat Transfer*, 106:699–706, November 1984.

[16] P.A. Gillis and P.J. Smith. An evaluation of three-dimensional computational combustion and fluid dynamics for industrial furnace geometries. In *Twenty-Third Symposium (International) on Combustion.* pp. 981-991, The Combustion Institute, 1990.

[17] S. Glasstone. *Thermodynamics for Chemists.* van Nostrand Co., Princeton, 1947.

[18] A.D Gosman, F.C. Lockwood, and A.P. Salooja. The prediction of cylindrical furnaces gaseous fueled with premixed and diffusion burners. In *Seventeenth Symposium (International) on Combustion.* pp. 747-760, The Combustion Institute, 1978.

[19] F. Harlow and J. Welch. Numerical calculation of time-dependent viscous incompressible flow of fluids with free surfaces. *Phys.Fl.*, 8:2182–2189, 1964.

[20] W.P. Jones and J.H. Whitelaw. Modeling and measurements in turbulent combustion. In *Twentieth Symposium (International) on Combustion.* pp. 233-249, The Combustion Institute, 1984.

[21] E.E Khalil. *Modeling of Furnaces and Combustors.* Abacus Press, 1982.

[22] E.E. Khalil, D.B. Spalding, and J.H. Whitelaw. The calculation of local flow properties in two-dimensional furnaces. *Int. J. Heat and Mass Transfer*, 18:775–791, 1975.

[23] M. Lai, J.B. Bell, and P. Colella. A projection method for combustion in the zero Mach number limit. In *Proceedings, AIAA 11nd Computational Fluid Dynamics Conference, Orlando, FL.* July 6-9, 1993, p.776-783, AIAA Paper 93-3369-CP.

[24] B.E. Launder and D.B. Spalding. The numerical computation of turbulent flows. *Comp. Meth. Appl. Mech. Eng.*, 3:269–289, 1974.

[25] E. E. Lewis and W. F. Miller, Jr. *Computational Methods of Neutron Transport.* American Nuclear Society, La Grange Park, IL, 1993.

[26] B.F. Magnussen and B.H. Hjertager. On the mathematical modeling of turbulent combustion with special emphasis on soot formation and combustion. In *Sixteenth Symposium (International) on Combustion, pp. 719-729, The Combustion Institute,1976.*

[27] A. Majda and J.A. Sethian. The derivation and numerical solution of the equations for zero Mach number combustion. *Combust. Sci. Tech.*, 42:185–205, 1985.

[28] B.R. Pai, S. Michelfelder, and D.B. Spalding. Prediction of furnace heat transfer with a three-dimensional mathematical model. *Int. J. Heat and Mass Transfer*, 23:571–580, 1978.

[29] S.V. Patankar. *Numerical Heat Transfer and Fluid Flow.* Hemisphere Publishing Corporation, 1980.

[30] S.V. Patankar and D.B. Spalding. A calculation procedure for heat, mass, and momentum transfer in three dimensional flows. *Int. J. Heat and Mass Transfer*, 15:1787–1806, 1972.

[31] D.G. Sloan, P.J. Smith, and L.D. Smoot. Modeling of swirl in turbulent flow systems. *Prog. Energy Combust. Sci.*, 12:163–250, 1986.

[32] L.D. Smoot and P.J. Smith. *Coal Combustion and Gasification.* Plenum Press, 1985.

[33] J.A. Trangenstein and J.B. Bell. Mathematical structure of the black-oil model for petroleum reservoir simulation. *SIAM J. Appl. Math.*, 49:749–783, 1989.

[34] R.J. Tucker and J.M. Rhine. *Modelling of Gas-Fired Furnaces and Boilers.* British Gas, McGraw-Hill, 1991.

[35] J.W. Watts. A compositional formulation of the pressure and saturation equations (SPE 12244). In *7th SPE Symposium on Reservoir Simulation.* San Francisco, CA, November, 1983, p.113-122.

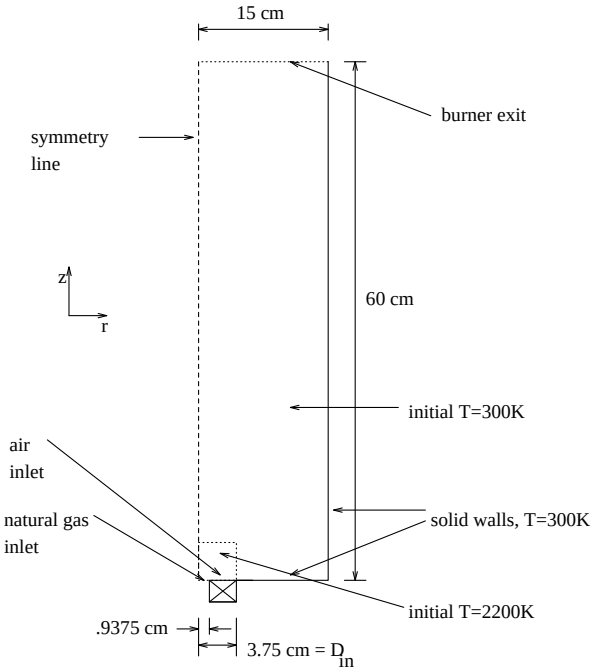

Figure 1: Configuration of burner for sample problem.

Figure 2: Computed solution of sample problem on a 32x128 grid at 1.53 sec. Temperature (°K), axial velocity (m/sec), and air mass fraction are shown.

Figure 3: Computed temperature (°K) of sample problem on a 16x64 grid at .075, .152, .763, and 1.53 sec.

Figure 4: Temperature (°K) of sample problem on a 16x64 grid at 1.53 sec for three computations using $A' = \infty$ (Arrhenius kinetics), $A' = 32.0$, and $A' = 4.0$, respectively.